A Wideband Low-Distortion CMOS Current Driver for Tissue Impedance Analysis

Loucas Constantinou, *Student Member, IEEE*, Richard Bayford, *Member, IEEE*, and Andreas Demosthenous, *Senior Member, IEEE*

***Abstract*—Bioimpedance measurements are performed in a variety of medical applications including cancer detection in tissue. Such applications require wideband (typically 1 MHz) accurate ac current drivers with high output impedance and low distortion. This paper presents an integrated current driver that fulfills these requirements. The circuit uses negative feedback to accurately set the output current amplitude into the load. It was fabricated in a 0.35-μm complementary metal–oxide–semiconductor (CMOS) process technology, occupies a core area of 0.4 mm^2, and operates from $\pm$2.5-V power supplies. For a maximum output current of 1 mA$_{p\text{-}p}$, the measured total harmonic distortion is below 0.1%, and the variability of the output current with respect to the load is below 0.5% up to 800 kHz increasing to 0.86% at 1 MHz. The current driver was tested for the detection of cancer sites from postoperative human colon specimens. The circuit is intended for use in active electrode applications.**

***Index Terms*—Active electrodes, bioimpedance, cancer detection, integrated current driver, low distortion, wideband.**

I. Introduction

BIOIMPEDANCE measurement techniques have been applied in the study of tissue electrical properties in a variety of clinical environments for many years. Tissue electrical properties exhibit frequency-dependent characteristics over a wide bandwidth (typically 100 Hz–1 MHz) [1]. The study of the electrical impedance characteristic of tissue provides useful information regarding tissue physiology and pathology [2], [3]. In the case of cancer, normal cells change in an uncontrolled way and can invade surrounding healthy tissue. Changes in tissue structure can be detected by changes in tissue impedance.

A widely used method for measuring bioimpedance is the tetrapolar electrode configuration. It involves applying an ac current through one pair of electrodes and measuring the resulting voltage potentials on a second pair of electrodes. Tissue impedance characteristics can be measured using techniques such as synchronous detection [4]. The ac current driver must have sufficient accuracy over the total operational bandwidth, and its output must be independent of load variations. As a result, the current driver requires a relatively high output impedance relative to the load and low distortion (total harmonic distortion; THD $< 0.5\%$ typically) particularly for multifrequency drive currents.

A variety of current drivers have been reported in the literature, mainly using discrete designs such as the Howland circuit [5]. Some designs have the addition of generalized impedance converter circuits to reduce the stray capacitance and boost the output impedance [6]. The Howland circuit does not lend itself easily to a fully integrated circuit implementation due to the requirement for very accurate resistors (< 0.1%). The targeted application (colorectal cancer detection) requires intimate contact of the current driver with the electrodes (i.e., active electrodes) for which an integrated circuit is well suited. The use of active electrodes significantly reduces the effect of cabling parasitic capacitance, which can reach a value up to 40–100 pF/m. Cancer detection requires that extracellular physiology is probed at low frequencies and intracellular physiology at high frequencies [7], hence the need for wideband operation, which is limited in existing integrated current drivers [8]–[10].

This paper concerns the design, implementation, and evaluation of an integrated current driver in complementary metal–oxide–semiconductor (CMOS) technology suitable for colorectal cancer (and other applications). The designed current driver uses negative feedback to accurately set the output current amplitude into the load and achieve a low THD. The architecture and circuits of the current driver and analysis of its linearity performance are described in Section II. Section III presents experimental evaluation of the fabricated current driver chip including both electrical bench tests and colorectal tissue impedance measurements. Section IV concludes this brief.

II. Circuit Design and Analysis

A. Current Driver Architecture

Fig. 1 shows the block diagram of the current driver. It uses two identical single-input differential-output current drivers (subdrivers), i.e., one for sinking current and the other for sourcing current to establish a balanced voltage across the load Z_L. This configuration cancels the common-mode voltage error across the load due to a voltage imbalance, caused by sense resistor R_{s1} (or R_{s2}), if a single current driver were to be used on its own (subdriver shown in Fig. 1). Each subdriver consists of a preamplification stage realized by a differential difference transconductance amplifier (DDTA$_1$ or DDTA$_2$), followed by a transconductor (G_{m1} or G_{m2}), which performs the voltage-to-current conversion operation and drives the load. An on-chip sense resistor (R_{s1} or R_{s2}) is used to monitor the output current

Manuscript received June 30, 2014; revised September 15, 2014; accepted November 28, 2014. Date of publication January 5, 2015; date of current version February 7, 2015. This work was supported by the U.K. Engineering and Physical Sciences Research Council (EPSRC) under Grant EP/G061629/1. This brief was recommended by Associate Editor G. Wang.

L. Constantinou and A. Demosthenous are with the Department of Electronic and Electrical Engineering, University College London (UCL), London WC1E 7JE, U.K. (e-mail: loucas.constantinou.10@ucl.ac.uk; a.demosthenous@ucl.ac.uk).

R. Bayford is with the Department of Natural Sciences, Middlesex University, The Burroughs, London NW4 4BT, U.K. (e-mail: r.bayford@mdx.ac.uk).

Color versions of one or more of the figures in this brief are available online at http://ieeexplore.ieee.org.

Digital Object Identifier 10.1109/TCSII.2014.2387632

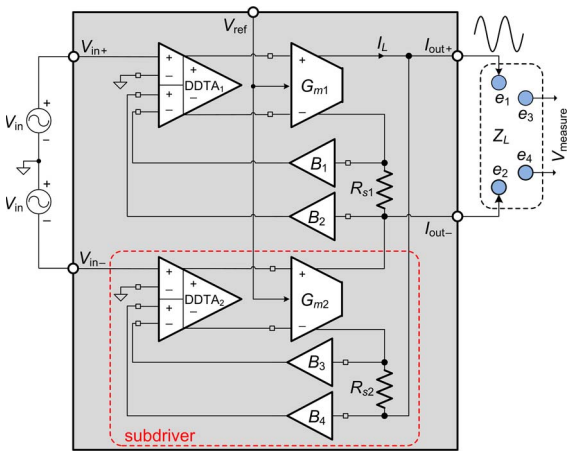

Fig. 1. Current driver architecture. Current is driven into the load Z_L, which consists of the electrodes e_1, e_2 and the tissue. Electrodes e_3 and e_4 are used to measure the resulting voltage potentials (i.e., tetrapolar configuration).

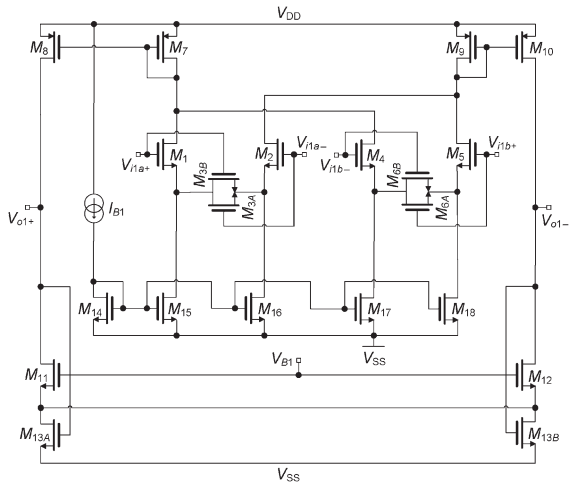

Fig. 2. DDTA transistor-level schematic.

I_L of each subdriver, and the voltage across the resistor is fed back via a pair of voltage buffers $[(B_1, B_2)$ or $(B_3, B_4)]$ to the appropriate terminals of the respective DDTA, thus forming a *negative*-feedback loop. The control voltage $V_{\rm ref}$ applied to G_{m1} and G_{m2} serves to accurately set the dc voltage levels at the two output nodes of the current driver (connected to electrodes e_1 and e_2 in Fig. 1). Although the basic principle has similarities with the current driver in [11], the emphasis has been to extend the operational bandwidth, reduce harmonic distortion, and lower the power supply voltage. An important added feature, which is absent in [11], is the control of the output dc offsets.

The low-frequency transfer function (i.e., transconductance) of each subdriver when the load is assumed to be a resistor R_L is given by

$$G_{\rm subdriver} = \frac{I_L}{V_{\rm in}} = \frac{1}{R_s + \left(\frac{r_o + R_s + R_L}{r_o}\right)\frac{1}{A_{\rm DDTA} G_m}} \tag{1}$$

where r_o and G_m are the small-signal output resistance and gain of the transconductor, respectively, and $A_{\rm DDTA}$ is the small-signal voltage gain of the DDTA. The negative-feedback loop will be mostly effective in the case where $r_o \gg R_s + R_L$ and $A_{\rm DDTA} G_m R_s \gg 1$. Thus, $G_{\rm subdriver} \approx 1/R_s$. Since two subdrivers operate in parallel (see Fig. 1), the total transconductance of the current driver (assuming matched devices) is $G_{\rm driver} \approx 2/R_s$. The low-frequency output resistance $R_{\rm out}$ of each subdriver due to the negative feedback is

$$R_{\rm out} = r_o + (A_{\rm DDTA} G_m r_o + 1) R_s. \tag{2}$$

The subdrivers in Fig. 1 operate in parallel, and the effective output resistance is reduced to $R_{\rm out}/2$, but the reduction can be offset by adjustment of $A_{\rm DDTA} G_m$ in (2).

B. DDTA

Fig. 2 shows the circuit schematic of the preamplification stage, which uses a fully differential topology. Transistors $M_1 - M_6$ form two differential pairs (input transconductance stage) whose output currents are summed at the drain of the diode-connected transistors M_7 and M_9. Transistors M_{3A-B} and M_{6A-B} provide source degeneration to enhance the input common-mode range. Current mirrors comprising transistor pairs $M_7 - M_8$ and $M_9 - M_{10}$ form a differential output stage with transistors M_{11} and M_{12}. This topology allows for independent control of the output stage of the circuit without affecting the input transconductance stage. Transistors M_{13A} and M_{13B} provide common-mode feedback control [12], and they are operated in the triode region. The differential output voltages V_{o1+} and V_{o1-} are approximately defined by

$$V_{o1+} \approx \left.\frac{g_{m1,4}(V_{i1a+} + V_{i1b-})}{g_{o8} + g_{o11}}\right|_{g_{m8} = g_{m7}} \tag{3}$$

$$V_{o1-} \approx \left.\frac{g_{m2,5}(V_{i1a-} + V_{i1b+})}{g_{o10} + g_{o12}}\right|_{g_{m10} = g_{m9}} \tag{4}$$

where g_{mi} and g_{oi}, respectively, represent the small-signal transconductance and output conductance of transistor i. The difference of V_{o1+} and V_{o1-} is the voltage across the sense resistor subtracted from the current driver input voltage $V_{\rm in}$.

C. Transconductor (G_m)

Fig. 3 shows the circuit schematic of the transconductor that uses a three-current-mirror operational transconductance amplifier (OTA) topology. The low-supply-voltage specification (5 V) of this design (compared with [11]) dictates the use of simple current mirrors with reduced overdrive voltage operation of the output transistors. Approximate output-dc-level stabilization uses triode transistors M_{16A} and M_{16B}. However, due to process variations, sufficiently accurate determination of the output common-mode level is not possible. Thus, transistors M_{15A} and M_{15B} whose gate voltages are controlled by (external) voltage $V_{\rm ref}$ are added in the secondary n-type metal–oxide–semiconductor (MOS) current mirror branches. Adjustment of $V_{\rm ref}$ alters the output dc levels. Care must be taken to ensure that $V_{\rm ref}$ holds M_{15A} and M_{16B} in the triode region.

Considering current mirror pair $M_{10} - M_{11}$ and triode transistors M_{15A} and M_{16B} (assuming that M_{15A} is in the triode region), the source voltages of M_{10} and M_{11} are given by

$$V_{s10} = V_{g10} - V_T - V_{ov10} = \frac{I_{d10}}{\beta_{15A}(V_{\rm ref} - V_{\rm SS} - V_T)} \tag{5}$$

$$V_{s11} = V_{g10} - V_T - V_{ov11} = \frac{I_{d11}}{\beta_{16B}(V_{o2\_q} - V_{\rm SS} - V_T)} \tag{6}$$

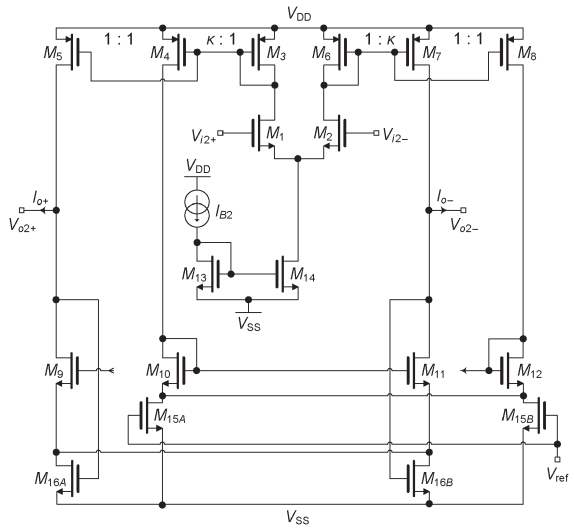

Fig. 3. Transistor-level schematic of the transconductor.

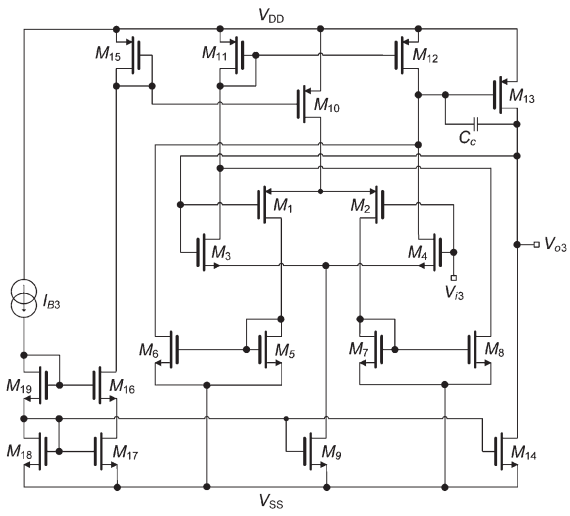

Fig. 4. Transistor-level schematic of the voltage buffer.

where V_g is the gate voltage, V_T is the threshold voltage, $V_{ov} = \sqrt{2I_d/\beta}$ is the overdrive (saturation) voltage, β is the process transconductance, I_d is the drain current, V_{o2_q} is the quiescent point of outputs V_{o2+} and V_{o2-}, $V_{\rm SS}$ is the negative supply voltage, and the subscript numbers in V_g, V_{ov}, and β refer to the respective transistors in Fig. 3.

Through current mirroring, the drain currents of M_{11} and M_{10} are (to a first-order approximation) equal. By ensuring that M_{15A} and M_{16B} are of equal dimensions, and using (5) and (6), the output dc voltage can be manually adjusted by $V_{\rm ref}$ in a linear fashion. However, current mirror nonidealities as well as the setting of $V_{\rm ref}$ that could drive M_{15A} (and M_{15B}) outside the linear region affect the accuracy of the setting. The output voltage compliance of the OTA is

$$V_{\rm SS} + V_{ds16A,B} + V_{ovM_{9,11}} < V_{o2} < V_{\rm DD} - V_{ov5,7} \qquad (7)$$

where $V_{\rm DD}$ is the positive supply voltage. The OTA voltage compliance was designed to be ± 2 V by ensuring low-saturation-voltage operation of the output transistors.

D. Voltage Buffer

Fig. 4 shows the circuit schematic of the voltage buffer. Transistors $M_1 - M_4$ form two complementary input differential pairs for enhanced input common-mode range, whereas current mirror pairs $M_5 - M_6$ and $M_7 - M_8$ sense the p-type MOS differential pair currents. Current mirror pair $M_{11} - M_{12}$ performs the differential to single-ended operation, whereas M_{13} and M_{14} form a second stage gain for enhanced open-loop gain. Capacitor C_c ensures a sufficient phase margin when the output is fed back to the negative input terminal for unity-gain operation. The voltage buffer offers a near rail-to-rail input voltage range of ± 2.3 V in order to accommodate the total OTA output swing.

E. Current Driver Nonlinearity

Negative feedback offers an advantage over output harmonic content. Considering a single current driver as a nonlinear two-input–one-output system using a preamplifier and a transconductor, the current generated from the transconductor can be evaluated as an output signal consisting of a fundamental frequency and contaminated with higher order harmonics content. Harmonic coefficients can be evaluated considering both open- and closed-loop operation.

1) Open-Loop Operation: The transconductor output current (see Fig. 3) can be approximated as

$$I_o (= I_{o+} - I_{o-}) \approx \kappa g_{m1,2} V_i \sqrt{1 - \left(\frac{V_i}{2V_{ov1,2}}\right)^2} \qquad (8)$$

where κ is the current mirror gain factor, and $V_i = (V_{i2+} - V_{i2-})$ is the transconductor input differential voltage supplied from the output of the preamplifier. Taking the first two terms of the Taylor series expansion of the square root term in (8), simplifies to

$$\sqrt{1 - \left(\frac{V_i}{2V_{ov1,2}}\right)^2} \approx 1 - \frac{1}{2}\left(\frac{V_i}{2V_{ov1,2}}\right)^2. \qquad (9)$$

The output current (8) is then given by

$$I_o \approx \kappa g_{m1,2} V_i - \frac{\kappa g_{m1,2}}{8V_{ov1,2}^2} V_i^3. \qquad (10)$$

Assuming $V_i = 2V_a A \cos \omega t$, where A is the open-loop gain of the preamplifier (which is assumed linear over the required input range), and V_a is the input signal amplitude, then (10) becomes

$$I_o \approx \left(a_1 - \frac{3a_3}{4}\right)\cos \omega t - \frac{a_3}{4} \cos 3\omega t \qquad (11)$$

where the coefficients a_1 and a_3 are

$$a_1 = 2\kappa g_{m1,2} A V_a \qquad (12)$$

$$a_3 = \frac{\kappa g_{m1,2} (A V_a)^3}{V_{ov1,2}^2}. \qquad (13)$$

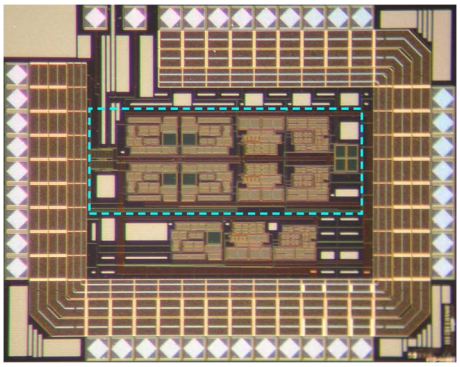

Fig. 5. Chip microphotograph. The area of the complete current driver (consisting of two subdrivers) is enclosed in the dashed rectangle.

2) Closed-Loop Operation: In the case of closed-loop operation (incorporating a sense resistor and a linear unity gain buffer in the feedback path as in Fig. 1), the signal to the negative input terminal of the transconductor is $V_{i2-} = AI_oR_s$, and (10) becomes

$$I_o \approx \kappa g_{m1,2}(V_{i2+} - AI_oR_s) - \frac{\kappa g_{m1,2}}{8V_{ov1,2}^2}(V_{i2+} - AI_oR_s)^3 \tag{14}$$

where R_s is the feedback sense resistor. The output signal can be also expressed as a Taylor series in which the signal to the transconductor positive input terminal (i.e., V_{i2+}) is the independent variable and assuming that when the input signal is zero, the output current is zero, the new coefficients are

$$a_1' = \frac{\kappa g_{m1,2}AV_b}{1 + \kappa g_{m1,2}AR_s} \tag{15}$$

$$a_3' = \frac{\kappa g_{m1,2}(AV_b)^3}{8V_{ov1,2}^2(1 + \kappa g_{m1,2}AR_s)^4} \tag{16}$$

where V_b is the new input signal amplitude ($V_b > V_a$ due to reduced gain) responsible for the same output current amplitude as in the open-loop case. The new coefficients show a reduction in their amplitude due to the action of the negative feedback. Simulations showed that for an output current of 300 μA_p at an input signal frequency of 500 kHz, closed-loop operation yields approximately 30 dB lower third harmonic distortion compared with open-loop operation. This explains the low distortion performance of the new current driver in comparison to other integrated current drivers [8]–[10] that are open-loop systems. Note that other sources of nonlinearity (e.g., in the preamplifier stage) will also be attenuated as a result of the closed-loop feedback.

III. Measured Results

A. Electrical Characterization

The current driver was fabricated in a 0.35-μm CMOS technology for operation from $\pm$2.5-V power supplies. Fig. 5 shows the die microphotograph. The core area of the current driver is 0.4 mm^2, and the total chip area including the pads and test structures is approximately 2.8 mm^2. The circuit design, simulations, and layout were developed with Cadence using the tool kit provided by the foundry. Each of the two on-chip sense resistors $R_{s1,2}$ were 500 Ω.

TABLE I
Measured Performance and Comparison

Parameter	[8]	[9]	[10]	This Work
Bandwidth	90 kHz	100–100 kHz	$\leq$1 MHz	$\leq$1 MHz
Output impedance	>560 kΩ @ 90 kHz	--------	>500 kΩ @ 500 kHz >160 kΩ @ 1 MHz	>1 MΩ @ 500 kHz, 360 kΩ @ 1 MHz
Max. output current	350 μA_{p-p}	400 μA_{p-p}	500 μA_{p-p}	1 mA_{p-p}
THD	<1% @ 250 μA_{p-p}	<0.2% @ 200 μA_{p-p}	0.79% @ 500 μA_{p-p}	<0.1% * @ 1 mA_{p-p}
Voltage compliance (Power supply)	>1.5 V (1.5 V)	0.4 V (1.8 V)	$\pm$1.8 V ($\pm$2.5 V)	$\pm$2 V ($\pm$2.5 V)

* Measured at 50 kHz. Simulations show that this value is attained at the maximum output current for frequencies up to 1 MHz.

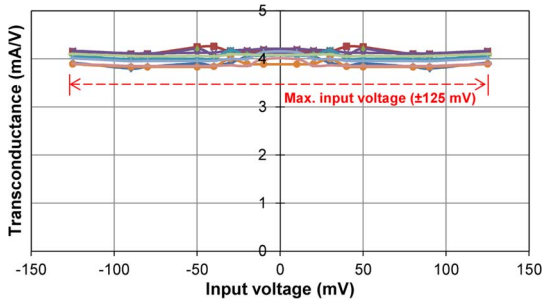

Fig. 6. Variation of transconductances of all chips versus input voltage at 10 kHz with a load of 1 kΩ||4.3 pF. The trasconductances are constant over the maximum input voltage range.

Nine chips were tested. Each chip was mounted on a custom printed circuit board providing the necessary bias currents and input/output signals to the circuit. The transconductance of the current driver over the required input voltage range and the accuracy of the output current over the frequency range 10 kHz to 1 MHz were examined. Other parameters such as output impedance and THD (measured with an SRS DS360 ultralow-distortion function generator) are listed in Table I.

Fig. 6 shows the measured transconductances for all chips at an operating frequency of 10 kHz with a load of 1 kΩ||4.3 pF. The input signals to the current driver were from a TTi TGA12101 signal generator. The maximum input signal of $\pm$125 mV should generate an output current of 1 mA_{p-p}. The measured average transconductance was 4.03 mA/V with a standard deviation from all the chips of 0.04 mA/V. The maximum spread between all nine chips was $\pm$1.45%.

The accuracy of the output current with different loads was measured using a series of saline tank experiments. A plastic circular tank (190 mm in diameter, 105 mm in height) containing sixteen 3-mm-diameter stainless steel electrodes (only four were activated) was filled with potassium chloride (KCl) solution of different conductivities (monitored by a HANNA HI 8733 conductivity meter) to represent different physiological entities [13]. The output current was measured for each conductivity value over the frequency range of 10 kHz–1 MHz. The injected current was measured by monitoring the voltage across a 100 Ω resistor in series with the load using an AD8253 instrumentation amplifier. The magnitude of the load impedance

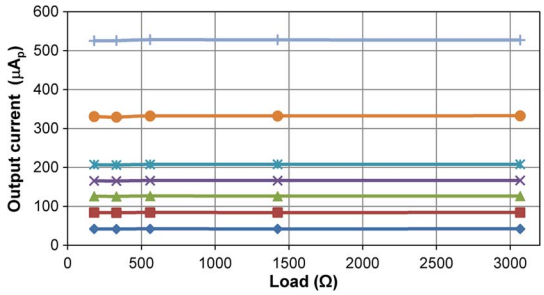

Fig. 7. Output current (I_{out}) amplitude for different saline load impedance values at 500 kHz. The solution conductivity values were 0.39, 0.86, 2.5, 5.07, and 15.65 mS/cm.

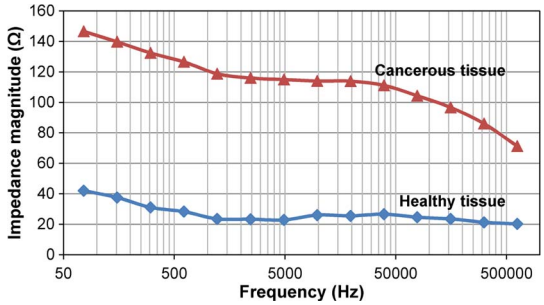

Fig. 8. Impedance magnitude spectra of healthy and cancerous tissue.

(electrode/electrolyte interface plus electrolyte) was measured using a Wayne Kerr 6500B impedance analyzer, for each value of conductivity between two adjacent electrodes. It was found to vary from 230 Ω to 3.1 kΩ. Fig. 7 shows the variation of the measured output current at 500 kHz for nominal values ranging from 40 μA_p to 500 μA_p. The change of the measured output current was approximately 0.34% up to 500 kHz increasing to 0.44% and 0.86% at 800 kHz and 1 MHz, respectively. The variation of the current between all nine chips was less than 1%.

B. Cancerous Tissue Detection

The current driver was mounted on a custom-made portable impedance measuring device to obtain impedance spectral characteristics of postoperative human colon tissue specimens diagnosed with cancer. The device employs a magnitude/phase approach [14] for tetrapolar impedance measurements. Interfacing of the device with the tissue used four (1.6 mm in diameter) silver electrodes (two for current injection and two for voltage measurement) distributed on a circular probe 5.5 mm in diameter. With ethics approval,[1] measurements on human tissue colon specimens were performed at two sites, i.e., one with advanced cancer development and another on healthy tissue 10 cm away. A current of 200 μA_p was injected in the frequency range between 76 Hz and 625 kHz (the variation of the current was better than 0.3% over this frequency range). Impedance magnitude spectra for both tissue sites are shown in Fig. 8. There was an almost fourfold increase in the measured impedance magnitude of the cancerous tissue relative to healthy tissue. A larger number of tissue samples, however, would need to be studied in order to establish the clinical usefulness of the method.

Table I provides a comparison with other low-voltage integrated current drivers. The new current driver features wide bandwidth, the largest output impedance, the highest output drive current, the best voltage compliance, and the lowest distortion.

[1]REC reference: 13/WM/0320, IRAS project ID: 135339.

IV. Conclusion

A wideband integrated current driver has been presented. It uses negative feedback to accurately set the output current amplitude into the load and achieve low distortion. The circuit was fabricated in a 0.35-μm CMOS technology and occupies a small silicon area of 0.4 mm^2. Its performance has been examined with a series of electrical bench tests and colorectal tissue measurements. The circuit is intended for active electrode realization capable of being mounted on clinical tools for real-time tissue impedance measurements.

References

[1] R. Bayford and A. Tizzard, "Bioimpedance imaging: An overview of potential clinical applications," *Analyst*, vol. 137, no. 20, pp. 4635–4643, Oct. 2012.
[2] R. J. Halter, A. Hartov, J. A. Heaney, K. D. Paulsen, and A. R. Schned, "Electrical impedance spectroscopy of the human prostate," *IEEE Trans. Biomed. Eng.*, vol. 54, no. 7, pp. 1321–1327, Jul. 2007.
[3] S. Abdul, B. H. Brown, P. Milnes, and J. A. Tidy, "The use of electrical impedance spectroscopy in the detection of cervical intraepithelial neoplasia," *Int. J. Gynecol. Cancer*, vol. 16, no. 5, pp. 1823–1832, Sep./Oct. 2006.
[4] R. Pallás-Areny and J. G. Webster, *Analog Signal Processing*. New York, NY, USA: Wiley, 1999.
[5] A. S. Tucker, R. M. Fox, and R. J. Sadleir, "Biocompatible, high precision, wideband, improved Howland current source with lead-lag compensation," *IEEE Trans. Biomed, Circuits Syst.*, vol. 7, no. 1, pp. 63–70, Feb. 2013.
[6] Y. Mohomadou *et al.*, "Performance evaluation of wideband bioimpedance spectroscopy using constant voltage source and constant current source," *Meas. Sci. Technol.*, vol. 23, no. 10, Oct. 2012, Art. ID. 105703.
[7] R. J. Halter, A. Hartov, and K. D. Paulsen, "A broadband high-frequency electrical impedance tomography system for breast imaging," *IEEE Trans. Biomed. Eng.*, vol. 55, no. 2, pp. 650–659, Feb. 2008.
[8] L. Yan *et al.*, "A 3.9 mW 25-electrode reconfigured sensor for wearable cardiac monitoring system," *IEEE J. Solid State Circuits*, vol. 46, no. 1, pp. 353–364, Jan. 2011.
[9] S. Hoo *et al.*, "A 4.9 mΩ-sensitivity mobile electrical impedance tomography IC for early breast-cancer detection system," in *Proc. IEEE ISSCC Dig. Tech. Papers*, San Francisco, CA, USA, 2014, pp. 316–317.
[10] H. Hong, M. Rahal, A. Demosthenous, and R. H. Bayford, "Comparison of a new integrated current source with the modified Howland circuit for EIT applications," *Physiol. Meas.*, vol. 30, no. 10, pp. 999–1007, Oct. 2009.
[11] L. Constantinou, I. F. Triantis, R. Bayford, and A. Demosthenous, "High-power CMOS current driver with accurate transconductance for electrical impedance tomography," *IEEE Trans. Biomed. Circuits Syst.*, vol. 8, no. 4, pp. 575–583, Aug. 2014.
[12] F. Krummenacher and N. Joehl, "A 4-MHz CMOS continuous-time filter with on-chip automatic tuning," *IEEE J. Solid-State Circuits*, vol. 23, no. 3, pp. 750–758, Jun. 1988.
[13] J. Wtorek, "Relations between components of impedance cardiogram analyzed by means of finite element model and sensitivity theorem," *Ann. Biomed. Eng.*, vol. 28, no. 11, pp. 1352–1361, Nov./Dec. 2000.
[14] P. Kassanos, I. F. Triantis, and A. Demosthenous, "A CMOS magnitude/phase measurement chip for impedance spectroscopy," *IEEE Sensors J.*, vol. 13, no. 6, pp. 2229–2236, Jun. 2013.